CrossMark

Surface topography measurements of the bouncing droplet experiment

Adam P. Damiano[1] · P.-T. Brun[1] · Daniel M. Harris[1] · Carlos A. Galeano-Rios[2,3] ·
John W. M. Bush[1]

Abstract A free-surface synthetic Schlieren (Moisy et al. in Exp Fluids 46:1021–1036, 2009; Eddi et al. in J Fluid Mech 674:433–463, 2011) technique has been implemented in order to measure the surface topography generated by a droplet bouncing on a vibrating fluid bath. This method was used to capture the wave fields of bouncers, walkers, and walkers interacting with boundaries. These wave profiles are compared with existing theoretical models and simulations and will prove valuable in guiding their future development. Specifically, the method provides insight into what type of boundary conditions apply to the wave field when a bouncing droplet approaches a submerged obstacle.

1 Introduction

A millimetric drop placed onto a vibrating liquid bath can bounce indefinitely on the fluid surface due to a thin film of air that prevents coalescence and is replenished with each bounce (Walker 1978; Couder et al. 2005; Terwagne et al. 2007; Vandewalle et al. 2006). The drop dynamics depends critically on the forcing acceleration of the bath γ relative to the critical threshold γ_F, at which the interface becomes unstable to Faraday waves. Couder et al. (2005) and Protière et al. (2006) discovered that in certain experimental regimes, the droplets may self-propel along the surface of the bath due to interactions with their own wave fields. These walking droplets, henceforth *walkers*, are spatially extended objects that exhibit several phenomena reminiscent of quantum systems (Couder and Fort 2006; Eddi et al. 2009, 2011; Bush 2010, 2015a, b; Fort et al. 2010; Harris et al. 2013; Perrard et al. 2014a, b; Oza et al. 2014; Harris and Bush 2014).

While the droplet, of typical radius 0.4 mm, is readily discerned by eye, the waves excited by the droplet, of typical amplitude of 1–20 µm, are relatively difficult to observe and quantify. Various theoretical models have been developed to describe the waves created by a bouncing droplet (Eddi et al. 2011; Molácek and Bush 2013a, b; Oza et al. 2013; Labousse 2014; Milewski et al. 2015; Gilet 2016; Blanchette 2016), on the basis of which much headway has been made in rationalizing the behavior of the walkers in a variety of settings [see Bush (2015a, b) for reviews]. Nevertheless, theoretical developments would benefit from quantitative measurements of the wave field. In particular, walker-boundary interactions as arise in a number of key quantum analogues (Couder and Fort 2006; Eddi et al. 2009; Harris et al. 2013; Harris 2015) remain poorly characterized and understood. Specifically, some theoretical models of walkers near boundaries apply a zero-wave-amplitude boundary condition (Gilet 2016; Blanchette 2016) while others apply a zero slope boundary condition (Dubertrand et al. 2016).

We here report the results of an experimental effort to measure the surface topography in the walking drop system using the surface synthetic Schlieren technique originally developed by Moisy et al. (2009), as was applied by Eddi et al. (2009, 2011). Specifically, we utilize the refracted

✉ P.-T. Brun
  pierrethomas.brun@gmail.com

[1] MIT, Cambridge, MA, USA

[2] IMPA/National Institute of Pure and Applied Mathematics, Est. D. Castorina, 110, Rio de Janeiro RJ 22460-320, Brazil

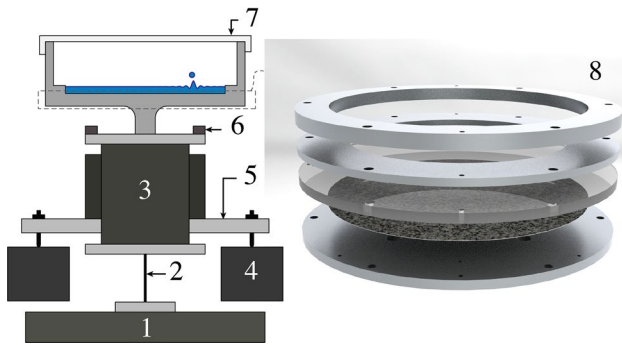[3] Department of Mathematical Sciences, University of Bath, Bath BA2 7AY, UK

Springer

Fig. 1 Layout of our experimental setup (Harris and Bush 2015) comprising an electromagnetic shaker (*1*) interfaced to the bath via a rod (*2*) and a linear air bearing (*3*). The air bearing carriage is fixed to an optical table (*4*) via a leveled platform (*5*). The bath acceleration is monitored via two accelerometers (*6*) and is surmounted by a lid (*7*). The bath (*8*) comprises a pattern printed on paper inserted below a transparent lower plate so that the pattern may be used as an imaging background

Fig. 2 The FSSS method (Moisy et al. 2009): **a** A sloped interface causes an apparent displacement of the points on a background image, $u(x, y)$. The refraction angle is denoted by ψ and the interface slope by ϕ. The background image is a random dot pattern (*b*) and the apparent displacement of the pattern creates a gradient field (*c*) that is used to reconstruct the surface topography (*d*)

image of a random dot pattern visualized through the interface to quantify the micrometric scale waves at the surface of the bath and adjoining its boundaries.

2 Experimental methods

The experiment consists of a bath of $\nu = 20$ cSt silicon oil vibrated sinusoidally at $\omega_0 = 80$ Hz with a peak acceleration γ (see Fig. 1). The apparatus is detailed in Harris and Bush (2015). The oil layer is typically 10–15 mm deep. Droplets are generated using piezoelectric actuation (Harris et al. 2015) and are 0.38 mm in radius. Unless otherwise specified, the range of accelerations γ used in experiments is such that the drop exhibits a period-doubled mode: Its impact phase relative to the vibrating bath may thus lie anywhere in the range 0°–720°. The experiments were recorded from above at 16 fps using a CCD camera (Manta G-125) placed at a height of $H = 1.1$ m from the bath that resolved an area of 55 × 74 mm and 964 × 1292 pixels. The same computer that drives the vibration of the bath was used to trigger the camera capture so that images at any phase of the driving cycle may be obtained.

The methodology employed to measure the waves in the system is the free-surface synthetic Schlieren (FSSS) method developed by Moisy et al. (2009). FSSS relies on the refraction of light and the apparent displacement of a random dot background image to infer the local slope of the fluid interface (Fig. 2). In our case, the background image was inserted beneath the 6.35-mm thick acrylic base plate of the bath (Fig. 1).

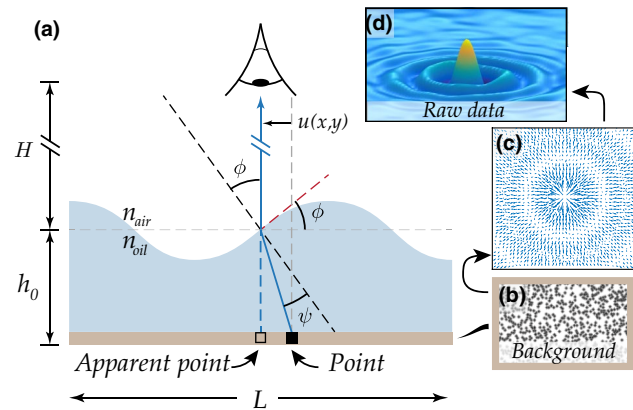We denote by $h(x, y, t)$ the height of fluid in the system. Given a reference image of the dot pattern obtained when

the bath is quiescent and the depth constant, $h = h_0$, and an image of the dot pattern when the surface has waves, digital image correlation is used to calculate the field displacement vectors, $\mathbf{u}$ (see Fig. 2b, c). These vectors are related to the gradient field, ∇h, of the interface. The inverse gradient of this field is used to reconstruct the surface height in the system via

$$h(x, y) = h_0 - \frac{\nabla^{-1}\mathbf{u}}{h_0(1 - n_{\text{air}}/n_{\text{oil}})}, \tag{1}$$

where n denotes the optical index of each phase. The surface cannot be resolved directly beneath the droplet, owing to its projected shadow. However, all conditions required for the validity of the FSSS method (Moisy et al. 2009) are satisfied by our system. Specifically, the distance from the camera to the background image, $H = 1.1$ m, is much larger that the field of view, of typical width 74 mm, thereby ensuring that the paraxial approximation is satisfied. The wave slope ϕ may be approximated as the ratio of the wave amplitude A and wavelength λ. In our system, $A < 25$ μm and $\lambda = 4.75$ mm yielding $\phi \simeq A/\lambda \ll 1$, so the weak-slope approximation required for the FSSS is satisfied (Moisy et al. 2009). Finally, the small-amplitude approximation is satisfied as deformations of the interface are of the order of microns while the fluid depth $h_0 \approx 10$ mm.

As the FSSS method resolves the fluid interface height based on small distortions of the background image, spurious inferred wave fields may be produced by small relative motions between the camera and the background image, as may originate, for example, as a result of vibrations associated with the camera ventilation system. In the present study, three filters are applied to the raw data in order to solve the aforementioned problem. Those filters are applied in the following order.

(a) *Horizontal surface filtering* Excluding waves excited by the droplet, the fluid surface remains horizontal since experiments are conducted below the Faraday threshold (Faraday 1831), $\gamma < \gamma_F$. However, ambient vibrations of the system contribute a mean translation to the gradient field, which results in a sloped fluid interface after surface height reconstruction. This spurious inference is filtered by removing any mean translation from the raw vector field, $\mathbf{u}^*$, before computing the inverse gradient via $\mathbf{u} = \mathbf{u}^* - \langle \mathbf{u}^* \rangle$. The final filtering is performed by subtracting the plane of best fit from the resulting wave field (see Supplementary Information for examples of the effect of this filtering step on raw data).

(b) *Rotation filtering* Similarly, vibrations also create small rotations between the camera and the background image, resulting in a spurious solid body rotation added to the gradient vector field. This rotation is likewise filtered by computing and subtracting out the mean solid body rotation from the gradient field. Setting the center of the field as the origin of a polar coordinate system, we denote each vector in the gradient field as $\mathbf{u}_i(r)$, where r is the distance from the origin. The angular rotation about the center of each vector is evaluated as

$$\Omega_i = \mathbf{u}_i \cdot \mathbf{e}_\theta / r. \tag{2}$$

where $\mathbf{e}_\theta$ is the unitary orthoradial polar vector. We evaluate the mean solid body rotation Ω as the average angular rotation of each vector (see Supplementary Information for examples of the effect of this filtering step on the data).

(c) *Band-pass filtering* The bouncing droplet generates a predominantly monochromatic wave field as the dominant sustained waves in the system are those at the Faraday wavelength (Molácek and Bush 2012). We thus selectively apply a band pass filter around the Faraday wavelength, $\lambda = 4.75$ mm in the bath, to remove high and low frequency noise (Gonzalez and Woods 2002). We convert the wave field into the spectral domain and then apply a 2D Butterworth filter before converting back into the spatial domain. For cases of variable bottom topology, the depth-dependence of the Faraday wavelength is such that λ typically decreases by 1 mm in shallow regions, where the depth is typically a fraction of a millimeter ($h_0 = 0.3$ mm with our obstacles). Our filtering thus adequately resolves waves in both the depth and shallow regions (see Supplementary Information for examples of the effect of this filtering step on the data).

3 Bouncer wave profiles

We first measured the axially symmetric wave field generated by a stationary bouncing droplet bouncing in $(2, 1)^2$ mode (see the star in Fig. 3). The inferred wave field is
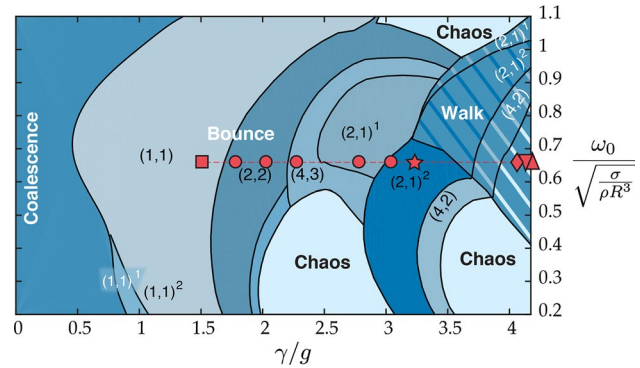

Fig. 3 Regime diagram [see Molácek and Bush (2013b) for its derivation] displaying the drop's bouncing or walking mode as a function of the vibration number $\omega_0/\sqrt{\sigma/\rho R^3}$ and driving acceleration γ/g. A drop in the $(m, n)^i$ mode bounces n times in m forcing periods, with the integer i ordering multiple (m, n) states according to their total mechanical energy, with $i = 1$ being the lowest. Here, we have $\omega_0 = 80$ Hz, $\nu = 20$ cSt and fixed drop radius $R = 0.38$ mm. The *red symbols* indicate the experiments performed in our study

shown in Fig. 4. These results are obtained using relatively small values of the acceleration, $\gamma \lesssim 0.78\,\gamma_F$ for our drops, so that the droplets, henceforth *bouncers*, do not propel themselves across the bath. Isocontours of the wave field are used to identify the droplet center location. We leverage the system's spatial and temporal periodicity to average our measurements (see Fig. 4).

By recording 24 videos at different phases of the bouncing cycle, the temporal evolution of the wave field created by a period-doubled bouncing droplet was resolved to 0.52 ms. A selection of waveforms at different phases of the bouncing cycle is presented in Fig. 4. The maximum recorded amplitude outside the shadow region in the entire bouncing cycle was 22 μm, less than 1 % of the droplet radius (0.38 mm). The amplitude of the waves evidently decays rapidly and is nearly indistinguishable from the mean surface height beyond four wavelengths from the center. The spatial decay rate is a function of the forcing acceleration: the stronger the forcing, the weaker the decay (Eddi et al. 2011).

Experiments were conducted to quantify the effect of the forcing acceleration on the amplitude of the waves excited by a bouncing droplet. The nondimensional forcing acceleration, γ/γ_F, was varied from 0.36 to 0.72, and the results are shown in Fig. 5. As expected, an increase in forcing acceleration increases the wave amplitude. At a greater forcing acceleration, the droplet bounces higher and a greater force is imparted to the fluid interface during impact. Moreover, the increased acceleration reduces the damping of the waves in both time and space.

Quantitative measurements of the wave profiles can be used to benchmark theoretical models. We find an excellent agreement between our experiments and the model
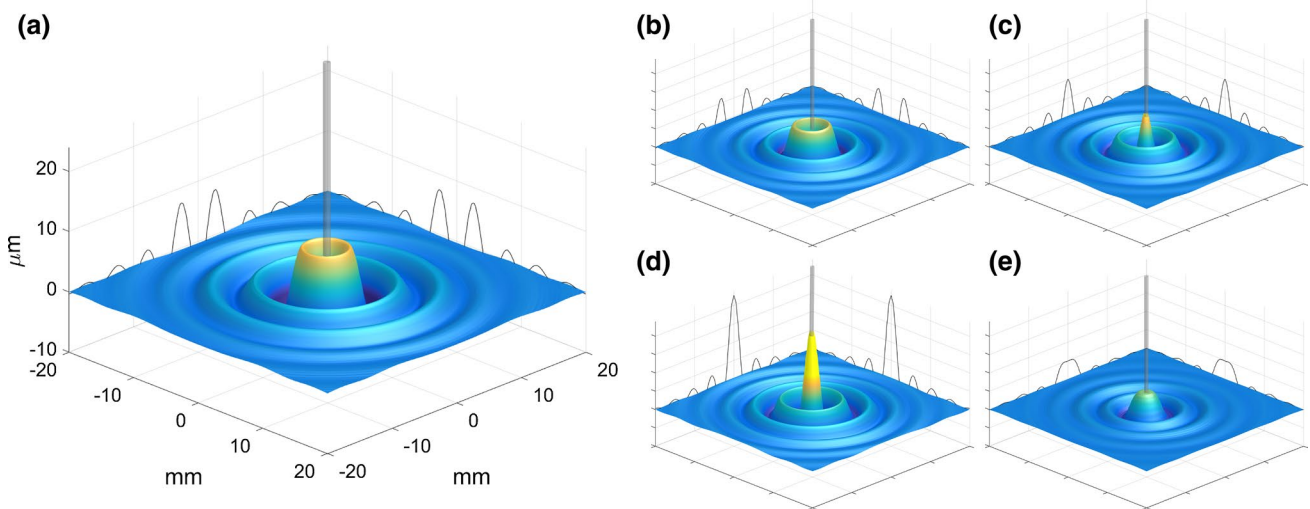
Fig. 4 Temporal evolution of the wave field excited by a period-doubled bouncing droplet of radius 0.38 mm. The acceleration of the 20 cSt oil bath is $\gamma = 0.77\,\gamma_F$ and $\omega_0 = 80\,\text{Hz}$ (see the *red star* in Fig. 3). The wave field is shown at phases **a** 0°, **b** 150°, **c** 300°, **d** 450° and **e** 600°. Phase 0° corresponds to the bath at its maximum vertical displacement. *Black lines* show a projection of the crosssection of the wave field passing through the droplet's center. The *gray cylinders* indicate the location of the droplet's projected shadow, where the wave field cannot be determined.
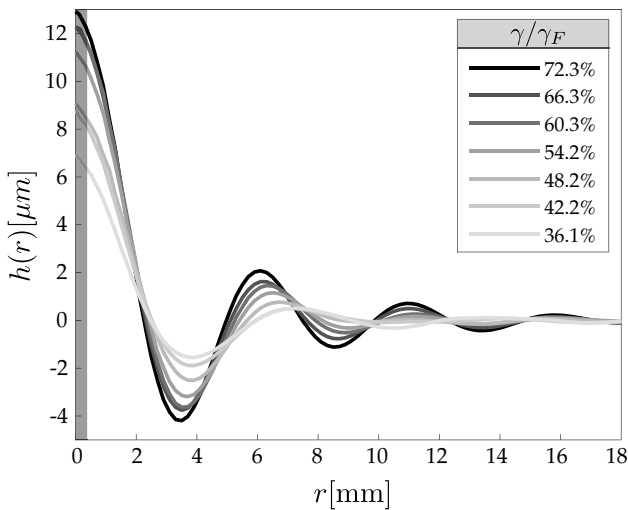

Fig. 5 Dependence of the wave profile of a bouncing droplet on the dimensionless forcing accelerations γ/γ_F where γ_F denotes the Faraday threshold. The drop radius is 0.38 mm, while $\omega_0 = 80\,\text{Hz}$ and $\nu = 20\,\text{cSt}$. Each experiment is represented by a dot in Fig. 3. The wave profile is captured when the bath is at its minimum vertical displacement. The *dark vertical band* in the vicinity of $r = 0$ represents the droplets projected shadow

reported in Molácek and Bush (2013b), which approximates the wave profile as the superposition of zeroth-order Bessel functions that decay exponentially in time while being spatially damped. Superposing the effects of each bounce one yields an infinite sum that may be replaced by an integral. After time integration and taking a mid-impact phase we find:

$$h(r) = 2A\sqrt{b}\,\mathbf{J}_0(k_F r)r\mathbf{K}_1(2\sqrt{b}r), \tag{3}$$

where $A = 12.6\ \mu\text{m}$ and $b = 0.0053\ \text{mm}^{-2}$ are computed following Molácek and Bush (2013b) and $k_F = 1.32\ \text{mm}^{-1}$ is the Faraday wave number [see Eq. (A.47) in Molácek and Bush 2013b for details].

Time-resolved wave profiles generated by simulation (Milewski et al. 2015) were also compared with the experimentally recorded wave profiles. The wave profiles agree well throughout the entirety of the bouncing cycle. One way that agreement is assessed is by analyzing the propagation characteristics of the zero-points of the wave profile where the surface height is equal to that in the undisturbed far field. This comparison is presented in Fig. 6b, and results again indicate strong agreement between simulation and experiments. A comparison of wave profiles throughout the entire bouncing cycle is included in the form of a video in Supplementary Information.

4 Walker wave fields

When the forcing acceleration exceeds the walking threshold, the droplet propagates across the bath in a straight line provided no obstacles are encountered (Protière et al. 2006; Oza et al. 2014). This walking threshold, which is a function of drop size, is $\gamma \approx 3.25$ g for
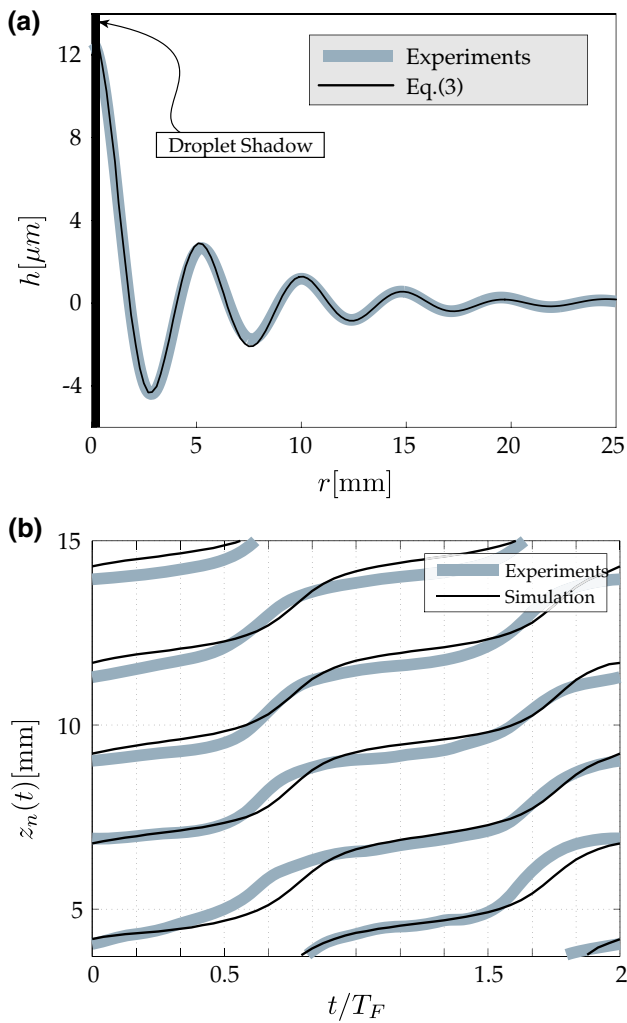
(a)

(b)

Fig. 6 Wave profiles generated by a droplet of radius 0.38 mm on a 20 cSt silicon oil bath with $\omega_0 = 80$Hz (see the star in Fig. 3). **a** Experimental results for $h(r)$ with $\gamma/\gamma_F = 0.77$, captured mid-impact (*thick line*). Also shown is the prediction obtained using the theoretical model of Molácek and Bush (2013b), which includes spatial damping, $r\mathbf{K}_1(2\sqrt{br})$, as indicated in Eq. (3). **b** Comparison between the motion of the zeros, z_n, of the wave profile in our experiments (*thick line*) and for numerical simulations (Milewski et al. 2015) (*thin line*). The dimensionless time is t/T_F, where T_F denotes the Faraday period

the present study (Wind-Willassen et al. 2013), for which $\gamma_F = 4.15$ g (see Fig. 3). Just above the walking threshold, the wave field of a walking droplet is nearly axially symmetric about the droplet location. Close to the Faraday threshold, conversely, parallel tracks of peaks and valleys extend behind the droplet. Between these two extremes, the walker produces a wave field that contains a checkered wake that may be found by superposing the low and high forcing acceleration wave fields (Eddi et al. 2011). The wave fields of walking droplets were recorded at a variety of phases and forcing accelerations. The comparison with simulation for a forcing acceleration of
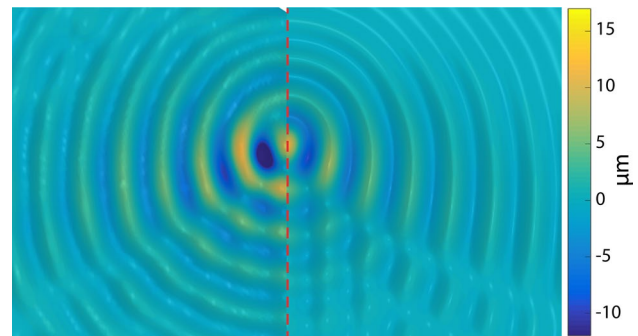

Fig. 7 Comparison between experimental data (*left*) and simulation (*right*) of the wave field excited for a walking droplet when the bath is at its maximum vertical displacement. Droplet radius is 0.38 mm, $\omega_0 = 80$ Hz, $\nu = 20$ cSt and $\gamma/\gamma_F = 0.966$ (as indicated by the diamond marker in Fig. 3). The comparison shows favorable agreement between the observed and predicted field structures, dominant wavelengths, and wave amplitudes, although the numerical simulations display a more pronounced interference pattern behind the droplet than observed in our experiments
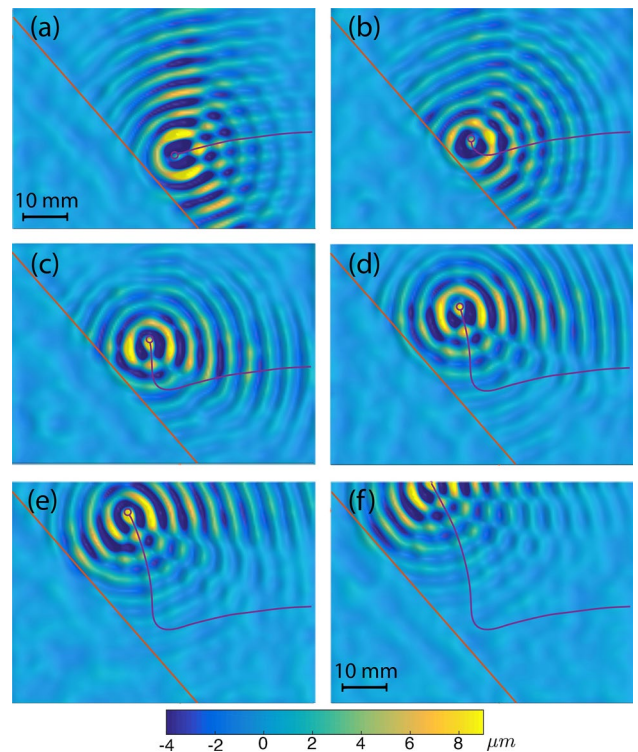

Fig. 8 Wave field of a walker (radius of 0.38 mm, $\omega_0 = 80$ Hz, $\nu = 20$ cSt) as it approaches and reflects from a planar, submerged barrier. The depth changes from $h_0 = 10$ mm in the deep region to $h_1 = 0.3$ mm over the barrier and $\gamma/\gamma_F = 0.979$ (downward pointing triangle in Fig. 3). Still video images from the video are presented in increments of 0.875 seconds and correspond to the bath at its maximum vertical displacement

$\gamma/\gamma_F = 0.966$ is presented in Fig. 7. The wave field of the walker was found to be consistent in terms of both amplitude and structure.
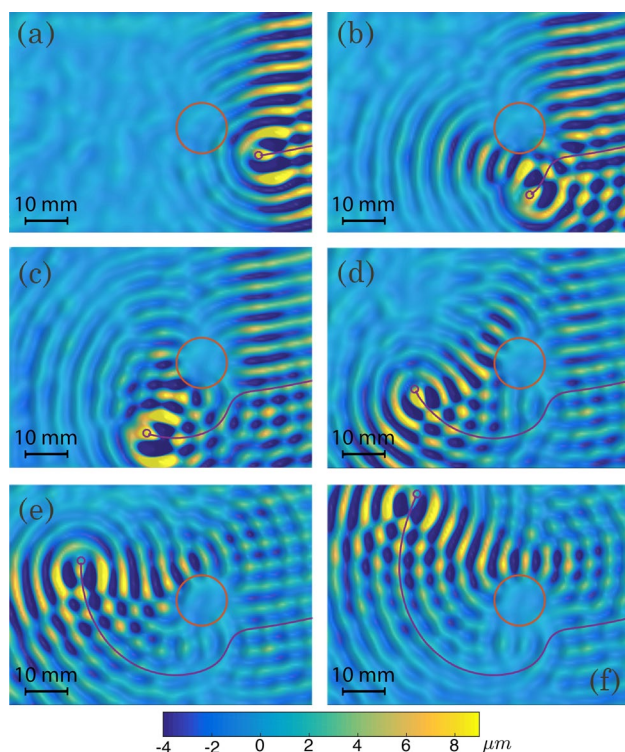
Fig. 9 Wave field of a droplet (radius of 0.38 mm, $\omega_0 = 80$ Hz, $\nu = 20$ cSt) as it approaches and spirals away from a circular, submerged pillar. The depth changes from $h_0 = 10$ mm in the deep region to $h_1 = 0.3$ mm over the pillar and $\gamma/\gamma_F = 0.995$ (upward pointing triangle in Fig. 3). Still video images are presented in increments of 1.625 s and correspond to the bath at its maximum vertical displacement

Walker-boundary interactions (Couder and Fort 2006; Eddi et al. 2009; Harris et al. 2013; Harris 2015) remain poorly understood and pose a challenge to theoreticians (Gilet 2016; Blanchette 2016; Dubertrand et al. 2016). In order to guide theoretical developments, we consider walkers interacting with relatively simple geometries, specifically, a planar boundary and a circular pillar.

A planar boundary was submerged 0.3 mm below the fluid bath interface, and walkers were directed toward the boundary. Waves transmitted over the boundary evidently die off quickly in the shallow area, typically on the order of a Faraday wavelength with our experimental parameters (see Fig. 8). At the step between shallow and deep regions, we observe that the wave field satisfies neither Dirichlet nor Neumann boundary conditions. This result suggests that obstacles should not be treated theoretically with a conventional boundary condition, but rather as an abrupt modification of the dispersion relation induced by the change of topography (Faria 2016). Note that for relatively deep and narrow obstacles, transmitted waves have been reported to persist long enough to occasionally transport the droplet across the barrier, thereby generating a quantum-like

tunneling effect (Eddi et al. 2009). In our case, owing to the relatively shallow and wide boundary, a reflection of the droplet is systematically observed (see Fig. 8). After the reflection, the droplet follows a curved trajectory that ultimately straightens out (Pucci 2016).

Walkers were also directed toward a submerged pillar, above which a similar damping of the waves is apparent (Fig. 9). Images of the wave field suggest that the trailing wake edge, specifically the curve of local maxima, is effectively tethered to the pillar, resulting in the spiral trajectory evident in Fig. 9.

5 Conclusion

The free-surface synthetic Schlieren method (Moisy et al. 2009) has been applied to the bouncing droplet experiment and was found to be effective in quantifying the surface waves of both bouncing and walking droplets. The wave profile of the bouncer was compared with mathematical models (Molácek and Bush 2013b) and simulations (Milewski et al. 2015) and was found to be in good agreement. These comparisons would seem to confirm the reliability of the method and demonstrate that it can be used successfully to benchmark existing theoretical models. Observations of the wave field as a walker interacts with boundaries offer new insights that will inform the development of accompanying theoretical models (Faria 2016).

References

Blanchette F (2016) Modeling the vertical motion of drops bouncing on a bounded fluid reservoir. Phys Fluids (1994-Present) 28(3):032104

Bush JWM (2010) Quantum mechanics writ large. Proc Natl Acad Sci 107:17455–17456

Bush JWM (2015) Pilot-wave hydrodynamics. Annu Rev Fluid Mech 47:269–292

Bush JWM (2015) The new wave of pilot-wave theory. Phys Today 68(8):47

Couder Y, Fort E, Gautier C-H, Boudaoud A (2005) From bouncing to floating: noncoalescence of drops on a fluid bath. Phys Rev Lett 94:177801

Couder Y, Protière S, Fort E, Boudaoud A (2005) Walking and orbiting droplets. Nature 437:208

Couder Y, Fort E (2006) Single-particle diffraction and interference at a macroscopic scale. Phys Rev Lett 97:154101

Dubertrand R, Hubert M, Schlagheck P, Vandewalle N, Bastin T, Martin J (May 2016) Scattering theory of walking droplets in the presence of obstacles. ArXiv e-prints

Eddi A, Fort E, Moisy F, Couder Y (2009) Unpredictable tunneling of a classical wave-particle association. Phys Rev Lett 102:240401

Eddi A, Sultan E, Moukhtar J, Fort E, Rossi M, Couder Y (2011) Information stored in Faraday waves: the origin of a path memory. J Fluid Mech 674:433–463

Faraday M (1831) On a peculiar class of acoustical figures: and on certain forms assumed by groups of particles upon vibrating elastic surfaces. Philos Trans R Soc Lond 121:299–340

Faria LM (2016) A model for Faraday pilot-waves over variable topography. Private communication

Fort E, Eddi A, Boudaoud A, Moukhtar J, Couder Y (2010) Path-memory induced quantization of classical orbits. Proc Natl Acad Sci 107(41):17515–17520

Gilet T (2016) Quantumlike statistics of deterministic wave-particle interactions in a circular cavity. Phys Rev E 93(4):042202

Gonzalez RC, Woods RE (2002) Digital image processing, 2nd edn. Prentice Hall, Upper Saddle River

Harris DM, Liu T, Bush JWM (2015) A low-cost, precise piezoelectric droplet-on-demand generator. Exp Fluids 56(4):83

Harris DM (2015) The pilot-wave dynamics of walking droplets in confinement. PhD thesis, Massachussets Institute of Technology

Harris DM, Moukhtar J, Fort E, Couder Y, Bush JWM (2013) Wave-like statistics from pilot-wave dynamics in a circular corral. Phys Rev E 88:011001

Harris DM, Bush JWM (2014) Droplets walking in a rotating frame. J Fluid Mech 739:444–464

Harris DM, Bush JWM (2015) Generating uniaxial vibration with an electrodynamic shaker and external air bearing. J Sound Vib 334:255–269

Labousse M (2014) Investigation of a path-memory dynamics: a theoretical trial. Université Pierre et Marie Curie UPMC Paris VI, Theses

Milewski PA, Galeano-Rios CA, Nachbin A, Bush JWM (2015) Farady pilot-wave dynamics. J Fluid Mech 778:361–388

Moisy F, Rabaud M, Salsac K (2009) A synthetic schlieren method for the measurement of the topography of a liquid interface. Exp Fluids 46:1021–1036

Molácek J, Bush WM (2012) A quasi-static model of drop impact. Phys Fluids 24:127103

Molácek J, Bush WM (2013a) Drops bouncing on a vibrating bath. J Fluid Mech 727:582–611

Molácek J, Bush WM (2013b) Drops walking on a vibrating bath: towards a hydrodynamic pilot-wave theory. J Fluid Mech 727:612–647

Oza AU, Rosales RR, Bush JWM (2013) A trajectory equation for walking droplets. J Fluid Mech 737:552–570

Oza AU, Harris DM, Rosales RR, Bush JWM (2014) Pilot-wave dynamics in a rotating frame. J Fluid Mech 744:404–429

Perrard S, Labousse M, Fort E, Couder Y (2014a) Chaos driven by interfering memory. Phys Rev Lett 113(10):104101

Perrard S, Labousse M, Miskin M, Fort E, Couder Y (2014b) Self-organization into quantized eigenstates of a classical wave-driven particle. Nat Commun 5:3219

Protière S, Boudaoud A, Couder Y (2006) Particle-wave association on a fluid interface. J Fluid Mech 554:85–108

Pucci G, Sáenz PJ, Faria LM, Bush JW (2016) Non-specular reflection of walking droplets. J Fluid Mech 804:R3

Terwagne D, Vandewalle N, Dorbolo S (2007) Lifetime of a bouncing droplet. Phys Rev E 76:056311

Vandewalle N, Terwagne D, Mulleners K, Gilet T, Dorbolo S (2006) Dancing droplets onto liquid surfaces. Phys Fluids 18:091106

Walker J (1978) Drops of liquid can be made to float on the liquid. What enables them to do so? Sci Am 238:151–158

Wind-Willassen Ø, Molàcek J, Harris DM, Bush JWM (2013) Exotic states of bouncing and walking droplets. Phys Fluids 25:082002